ARTICLE

Digital Control of SiO_2-TiO_2 Mixed-Metal Oxides by Pulsed PECVD

Pieter C. Rowlette and Colin A. Wolden*

Department of Chemical Engineering, Colorado School of Mines, Golden, Colorado 80401

ABSTRACT Pulsed plasma enhanced chemical vapor deposition (PECVD) was used to deliver digital control of SiO_2, TiO_2, and SiO_2-TiO_2 composites at room temperature. Alloy formation was investigated by maintaining constant delivery of $TiCl_4$ while varying the $SiCl_4$ flow. Film composition was assessed by spectroscopic ellipsometry, XPS, and FTIR. It is shown that the alloy composition and refractive index can be tuned continuously over a broad range using pulsed PECVD. The two precursors were found to be highly compatible, with the alloy growth rate simply reflecting the sum of the contributions from the two individual precursors. Digital control over both thickness and composition was demonstrated through the production of antireflection (AR) coatings for crystalline silicon. AR coatings were synthesized on the basis of optimized designs, and in each case the measured optical performance was found to be in excellent agreement with model predictions. The average reflectance across the visible spectrum was reduced from 39% for uncoated wafers to 2.5% for the three-layer AR coating.

KEYWORDS: pulsed PECVD, TiO_2 • SiO_2 • alloy • anitreflection coating

1. INTRODUCTION

Pulsed plasma-enhanced chemical vapor deposition (PECVD) is an alternative to atomic layer deposition (ALD) for self-limiting growth of metal oxides. Pulsed PECVD has been successfully demonstrated for a number of binary oxides, including Ta_2O_5 (1, 2), Al_2O_3 (3, 4), and ZnO (5). In pulsed PECVD the metal precursor and O_2 are mixed and delivered simultaneously. Growth occurs discretely by modulating the plasma power at low frequency (~0.1−2 Hz). The nature of self-limiting growth is fundamentally different than that of ALD. Instead of relying on surface chemistry, growth terminates during each plasma step due to complete consumption of the precursor. The process has been demonstrated to deliver digital control over film thickness and produce a high degree of conformality at significant rates (>30 nm/min) (6, 7). More details on the pulsed PECVD process have been described in previous work (7, 8).

We have recently extended pulsed PECVD to the synthesis of SiO_2 (9) and TiO_2 (10) using halide precursors ($SiCl_4$, $TiCl_4$). An advantage of this chemistry is the absence of HCl or H_2O production, which is critical for vacuum processing at low temperatures. SiO_2 and TiO_2 are two of the most common materials employed in optical coatings, due to their chemical stability and large range of refractive indices (n = 1.4−2.6) (11−14). While stacks of individual oxides are employed for many applications, including optical filters (15−18) and antireflection (AR) coatings (11−14, 19), it is often desirable to tune the index of individual layers to intermediate values. In this work we show that pulsed PECVD can be effectively used for the formation of SiO_2-TiO_2 alloys using $SiCl_4$ and $TiCl_4$. Control of film composition and thickness is demonstrated through the fabrication of AR coatings for crystalline silicon solar cells. Silicon photovoltaics typically employ hydrogenated silicon nitride (SiN_x:H) deposited at temperatures between 350 and 450 °C as the AR coating (20−22). The SiN_x:H coatings are synthesized by PECVD, and the refractive index can be tuned from 1.9 to 2.4 by altering the H_2 flow rate (21). This allows single-layer SiN_x:H coatings to achieve zero reflectance at one wavelength. However, the relatively limited range of refractive indices makes it challenging to construct multilayer SiN_x:H coatings that further reduce the reflectance over the full visible spectrum. AR coatings are critical to achieving optimum performance, enhancing efficiency by as much as 40% (14, 23). In this work we focus on room-temperature synthesis, which is compatible with both the move to thinner Si wafers and emerging thin film technologies.

2. EXPERIMENTAL SECTION

2.1. Materials. The reactor used to deposit the SiO_2-TiO_2 alloys in this work is a parallel-plate, capacitively-coupled system that has been described in detail previously (6). The precursors for the individual materials were silicon tetrachloride ($SiCl_4$) and titanium tetrachloride ($TiCl_4$), respectively. Details on the synthesis of the pure SiO_2 (9) and TiO_2 (10) films are presented elsewhere. SiO_2-TiO_2 alloys were deposited by introducing both metal precursors to the reactor along with Ar and O_2 gases while modulating the plasma power at low frequency (~0.25 Hz). Si wafers treated with an HF dip were used as substrates.

$TiCl_4$ was delivered using a temperature-controlled bubbler (−10 °C) and argon carrier gas. Under the conditions used, the $TiCl_4$ flow rate was fixed at 0.3 standard cubic centimeters per minute (sccm). The Ar and O_2 flow rates were fixed at 240 sccm and 310 sccm, respectively. Due to its high vapor pressure, it was not possible to adequately control $SiCl_4$ flow rates using a bubbler. To achieve digital

Received for review July 29, 2009 and accepted October 6, 2009

DOI: 10.1021/am900506y

© 2009 American Chemical Society

Published on Web 10/19/2009

control over SiO_2 growth with angstrom-level resolution, $SiCl_4$ was pulsed into the reactant stream by opening an electronic valve on a fixed control volume. The amount of $SiCl_4$ was controlled by adjusting the duration of this pulse, as described previously (9). The $TiCl_4/SiCl_4/Ar/O_2$ streams were mixed and delivered to the reactor through a showerhead, which also served as the powered electrode. The reactor pressure was maintained at 0.60 Torr. The plasma power was set to 100 W, and the plasma on time was kept constant at 3 s for all experiments. The system was not heated and remained at ambient conditions (~25 °C) for all depositions. Multiple samples were grown to determine the reproducibility associated with the deposition process. It was found that the variation in growth rate was <3.0% while the refractive index changed <1% between identical depositions.

Spectroscopic ellipsometry (SE, J. A. Woollam) was used to determine the thickness and refractive index of the as-deposited films. Measurements were taken at an angle of 70°, and data were collected over the range of 450–1300 nm to ensure that the measurements were performed at energies below the TiO_2 band gap. A simple Cauchy model (24) was used to determine the refractive index and thickness of the films. Throughout this work, the refractive index is reported at 550 nm. Fourier transform infrared spectroscopy (FTIR, Nicolet Nexus 870) was performed on as-deposited samples to determine the film composition. Scans were taken from 400 to 4000 cm^{-1}, and the silicon substrate background was subtracted so that the FTIR spectra presented here reflect only the deposited films. X-ray photoelectron spectroscopy (XPS, Kratos) was performed using an Al Kα X-ray source. The base pressure of the analysis chamber was $<10^{-9}$ Torr, and high-resolution spectra of individual binding states were recorded using a scan time of 60 s at a pass voltage of 40 eV. For species of low concentration seven scans were performed, while three to five scans were used for species that were present in higher concentrations. Reflectance measurements were performed using a Cary 5G UV–vis–near-IR spectrophotometer at normal incidence.

2.2. AR Coating Design. The design for a single layer was carried out for normally incident light by examining the transfer matrix, $\mathbf{M}_1$, as discussed by Pedrotti et al. (25), which is shown below:

$$\mathbf{M}_1 = \begin{bmatrix} \cos\delta & \dfrac{\sin\delta}{i\gamma_1} \\ i\gamma_1 \sin\delta & \cos\delta \end{bmatrix} = \begin{bmatrix} m_{11} & m_{12} \\ m_{21} & m_{22} \end{bmatrix} \tag{1}$$

$$\delta = \frac{2\pi}{\lambda_o} n_1 t_1 \tag{2}$$

where λ_o is the wavelength of light examined, in this case 550 nm, n_1 is the refractive index of layer 1, and t_1 is the thickness of layer 1. For normal incidence, γ_1 is given by:

$$\gamma_1 = n_1\sqrt{\varepsilon_o \mu_o} \tag{3}$$

where n_1 is as defined above, ϵ_o is the permittivity of free space, and μ_o is the permeability of free space. These values can then be used to define the reflection coefficient, r:

$$r = \frac{\gamma_o m_{11} + \gamma_o \gamma_s m_{12} - m_{21} - \gamma_s m_{22}}{\gamma_o m_{11} + \gamma_o \gamma_s m_{12} + m_{21} + \gamma_s m_{22}} \tag{4}$$

where γ_o and γ_s are as defined in eq 3, substituting the refractive index of the incident medium (air, $n_o = 1.0$) and the substrate (Si, $n_s = 3.9$), respectively. The reflection coefficient can be grouped into both real and imaginary parts in the numerator and denominator, represented by eq 5:

$$r = \frac{A + iB}{C + iD} \tag{5}$$

and the reflectance, R, can then be determined from

$$R = |r|^2 = rr^* = \left(\frac{A + iB}{C + iD}\right)\left(\frac{A - iB}{C - iD}\right) = \frac{A^2 + B^2}{C^2 + D^2} \tag{6}$$

For normal incidence and a film of quarter-wave thickness, $t_{\lambda/4}$, which is defined as

$$t_{\lambda/4} = \frac{\lambda_o}{4n_1} \tag{7}$$

R reduces to

$$R = \left(\frac{n_o n_s - n_1^2}{n_o n_s + n_1^2}\right)^2 \tag{8}$$

From eq 8, it can be seen that to achieve zero reflectance at a given wavelength, λ_o, the AR coating must have the refractive index $n_1 = \sqrt{n_o n_s}$. To achieve zero reflectance at $\lambda_o = 550$ nm for a crystalline Si substrate in air, eqs 7 and 8 require a refractive index of $n_1 \sim 1.98$ and a thickness of $t \approx 69$ nm.

For multilayer coatings, the same equations as discussed above apply, except the transfer matrix is now defined as the product of the individual matrices:

$$\mathbf{M}_T = \mathbf{M}_1 \mathbf{M}_2 \mathbf{M}_3 \ldots \mathbf{M}_n \tag{9}$$

where M_T is the total transfer matrix for all layers, M_1 is the transfer matrix for the top layer in contact with the incident medium (air), M_2 and M_3 are the subsequent layers getting closer to the substrate with increasing numbers, and M_n is the final layer directly in contact with the substrate. In this

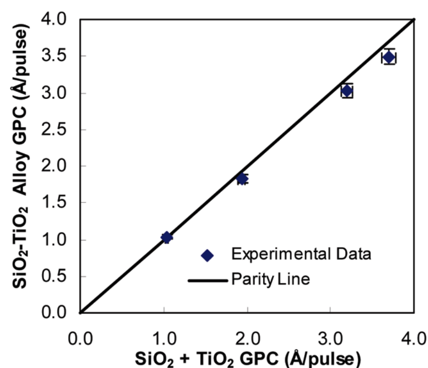

FIGURE 1. SiO_2-TiO_2 alloy GPC versus the sum of the individual SiO_2 and TiO_2 GPCs.

work, computer software (TFCalc (26)) was used to optimize both the indices and the thickness of multilayer AR coatings, and the above equations were then used to model the reflectance as a function of wavelength.

3. RESULTS AND DISCUSSION

Using only the $TiCl_4$ precursor under the conditions employed, it was found that TiO_2 was deposited at a growth per cycle (GPC) of 0.85 Å/pulse and had a refractive index of 2.3. This relatively low index suggests that the TiO_2 is amorphous, which was confirmed by X-ray diffraction. To form SiO_2-TiO_2 alloys, the $TiCl_4$ flow rate was held constant and variable amounts of $SiCl_4$ were introduced. Pure SiO_2 films were found to have a refractive index of 1.42, which is slightly less than the standard value of 1.46. The refractive index has been correlated to film density, and this value suggests that the films deposited in this work may have a small level of porosity.

In this work it was found that the growth rate of the alloys simply reflected the sum of the individual constituents. That is, if the density of each precursor was adjusted to produce 1 Å/pulse of the individual oxides, when the identical quantities were mixed together they produced ~2 Å/pulse of the SiO_2-TiO_2 alloy. This relationship is shown in Figure 1, which is a parity plot comparing the GPC observed during alloy growth with the sum of the GPCs obtained when each precursor was supplied individually. Deviations form the parity line increase with GPC but never exceed 5% even at the highest rate. Interestingly, the GPC of the alloys is systematically lower than the value obtained by adding the GPCs of the individual oxides.

These results demonstrate that in pulsed PECVD it is relatively straightforward to control the composition of mixed-metal oxides. In contrast, the relationship between film composition and precursor composition in conventional PECVD is highly nonlinear (13). Likewise, co-sputtering of SiO_2-TiO_2 alloys requires empirical optimization of the individual target conditions in order to control film composition (11). The linear relationship observed here is attributed to the extremely dilute conditions employed by pulsed PECVD to achieve self-limiting growth. The fraction of precursor supplied in the gas phase is well below 1%; thus, when multiple precursors are supplied their interactions remain minimal.

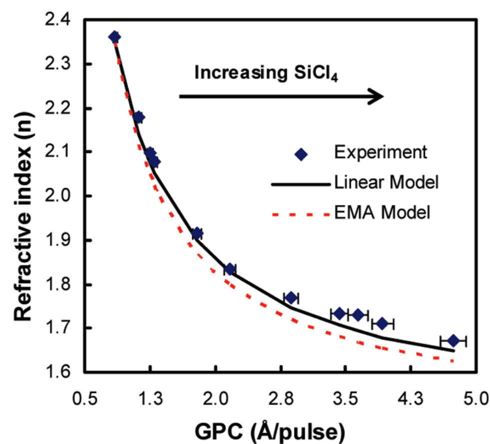

FIGURE 2. Refractive index (diamonds) vs GPC of SiO_2-TiO_2 alloys compared with predictions of the linear (solid line) and EMA (dashed line) models.

Figure 2 plots the refractive index as a function of GPC as increasing amounts of $SiCl_4$ were introduced to the system. The diamonds represent the experimental data, which show that the index gradually decreases as $SiCl_4$ was added to the system. A simple phenomenological model was developed to describe the observed changes in refractive index. The solid line in Figure 2 is based on the expression

$$n = xn_{TiO2} + (1 - x)n_{SiO2} \tag{10}$$

where n is the refractive index of the SiO_2-TiO_2 alloy, x is the volume fraction of TiO_2 in the film, n_{TiO_2} is the refractive index of pure TiO_2, and n_{SiO_2} is the refractive index of pure SiO_2. On the basis of the relationship shown in Figure 1, the volume fraction of TiO_2 (x) was calculated by dividing the GPC of pure TiO_2 (0.85 Å/cycle) by the total GPC of the SiO_2-TiO_2 alloy. As can be seen in Figure 2, this simple linear model fits the experimental data quite well. There was slight deviation from this model as the deposition rate increased, but the difference was within 2% at the highest GPC values. The dashed line in Figure 2 is the prediction of the Bruggeman effective medium approximation (EMA). The EMA model assumes that the composite films are a well-dispersed mixture of the pure SiO_2 and TiO_2 components. The EMA model underpredicts the experimental data, and this failure suggests that the SiO_2-TiO_2 films are homogeneous alloys and not a mixture of separate phases. The idea of alloy formation is supported by the characterization results that follow and is in agreement with published literature (13).

The film composition in this work was assessed by both FTIR and XPS. Figure 3 plots the FTIR spectra obtained from pure TiO_2, SiO_2, and selected alloy films. The spectra are normalized with respect to film thickness and offset for clarity. Note that no significant vibrations were observed at wavenumbers >1300 cm^{-1} and that part of each spectrum is excluded for clarity. An FTIR scan of pure SiO_2 is shown at the top of Figure 3 ($n = 1.42$). The dominant SiO_2 peaks include the asymmetric stretching (1070 cm^{-1}), symmetric stretching (805 cm^{-1}), and rocking (450 cm^{-1}) modes associated with the Si−O−Si groups.

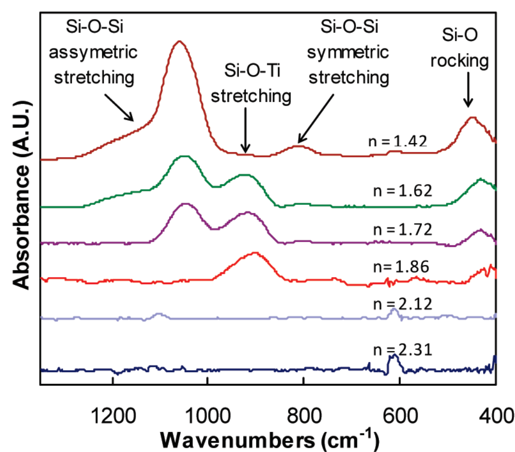

FIGURE 3. FTIR spectra of pure SiO_2, TiO_2, and selected SiO_2-TiO_2 alloys as a function of refractive index.

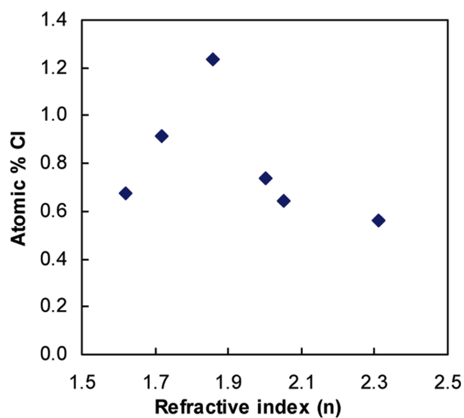

FIGURE 4. Atomic percent of Cl in as-deposited films as a function of refractive index.

The FTIR spectrum for the pure TiO_2 sample (Figure 3, $n = 2.31$) had no significant features. A notable absence is the vibration centered at 434 cm^{-1}, which is indicative of a crystalline, anatase phase (10, 27−29). This provides further confirmation that the TiO_2 deposited at room temperature in this work is amorphous. Alloy films containing small amounts of SiO_2 ($n = 2.12$) show no notable features, akin to the pure TiO_2 spectrum. As more SiO_2 is incorporated into the film, a peak at ∼930 cm^{-1} appears ($n = 1.86$). The peak present at ∼930 cm^{-1} has been assigned to Si−O−Ti stretching modes of SiO_2-TiO_2 single-phase mixtures (13). This assignment was originally identified in studies of titanium−silicate catalysts (30, 31). As the alloys become dominated by SiO_2 ($n \leq 1.72$), the normal SiO_2 features discussed above appear and begin to dominate the alloy spectra.

A potential contaminate in the SiO_2-TiO_2 alloys produced in this work is Cl, due to its presence in both metal precursors. Film composition was investigated using XPS analysis. Figure 4 shows the percent Cl contained in as-deposited films before sputter cleaning as a function of refractive index for SiO_2-TiO_2 alloys. Due to the fact that the XPS analysis was performed ex situ, there was a significant amount of C present due to surface contamination. This carbon signal was excluded from the composition analysis reported here. The chlorine content was quite low (< 1%) and generally

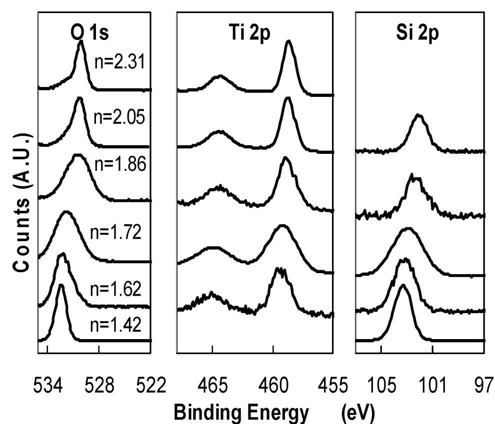

FIGURE 5. High-resolution O 1s, Ti 2p, and Si 2p XPS spectra of pure SiO_2, TiO_2, and selected SiO_2-TiO_2 alloys as a function of refractive index.

unchanged as the refractive index decreased from 2.3 to 1.55. Films with an intermediate composition had higher values, suggesting that the Si−Ti−O alloy phase may be somewhat more susceptible to Cl incorporation relative to the pure oxides.

High-resolution XPS scans of the O 1s, Ti 2p, and Si 2p regions were analyzed to more thoroughly investigate the bonding structure present in the pure and alloy films. These spectra are displayed in Figure 5, plotted as a function of film composition, which is ordered from pure SiO_2 at the bottom to pure TiO_2 at the top of the figure. The O 1s peak of the pure TiO_2 film ($n = 2.31$) is centered at a binding energy of 530.0 eV. As Si is added to the composite, the O 1s peak shifts to higher binding energies until it reaches a value of 532.3 eV for pure SiO_2. As the metal atom (M) associated with the M−O bond, in this case Si, is further to the right and up on the periodic table, the O 1s peak shifts to higher binding energies (32, 33), and this shift has been attributed to an increase in the ionicity of the M−O bonds in the oxide system (32, 33). This same trend is evident for both the Ti 2p and Si 2p peaks.

The addition of Si to the alloy mixture and the accompanying shift to higher binding energies also coincides with a broadening of the O 1s, Ti 2p, and Si 2p peaks (Figure 5). Examining the O 1s peak specifically, the full width at half maximum (FWHM) increases from 1.5 eV for pure TiO_2 to 1.86 eV for the alloy mixture shown in Figure 4 that had a refractive index of $n = 1.86$. This alloy with the maximum FWHM is approximately a 50:50 mixture of SiO_2 and TiO_2, according to the linear model shown in eq 10. As the alloys become dominated by Si ($x_{SiO_2} > 0.50$), the FWHM begins to decline, and it decreases to a value of 1.55 eV for pure SiO_2. Broadening of the FWHM in SiO_2-TiO_2 mixtures has been associated with the different contributions from O atoms bonded to two Si atoms, two Ti atoms, or one of each (13). The trend observed in the FWHM values is consistent with the presence of multiple bonding states. As the mixture composition deviates in either direction from the 50:50 mixture, the bonding composition becomes more homogeneous, resulting in a decreased FWHM. These XPS results

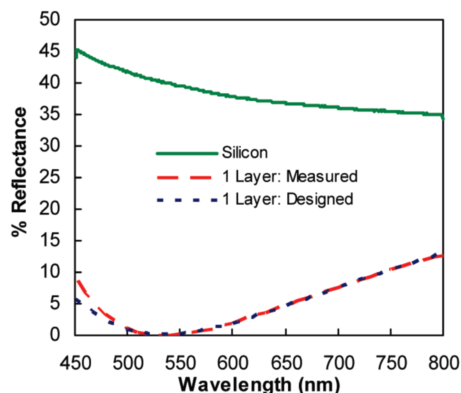

FIGURE 6. Percent reflectance versus wavelength for a blank silicon wafer (solid green line), a one-layer SiO_2-TiO_2 AR coating (dashed red line), and its theoretical design (dotted blue line).

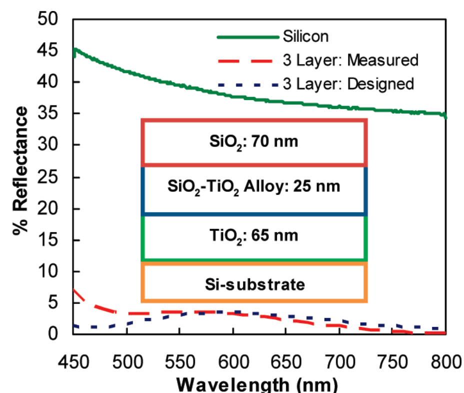

FIGURE 7. Percent reflectance versus wavelength for a blank silicon wafer (solid line), a three-layer AR coating (dashed red line), and its theoretical design (dotted blue line).

are also consistent with changes in the intensity of the Si−Ti−O stretching mode observed by FTIR.

One- and three-layer AR coatings were synthesized by pulsed PECVD to demonstrate the technique's digital control over both thickness and composition. The zero reflectance criteria at a wavelength of λ_o 550 nm requires a single layer with an index of 1.98 and a thickness of 69 nm. Figure 6 compares the measured reflectance with model expectations for the single-layer AR coating, and these results are compared to those for an uncoated Si wafer. The uncoated Si wafer has an average reflectance of 39% over the range 450−800 nm. It can be seen that the single-layer AR coating drastically reduces the reflectance over that of the blank wafer. Comparing the theoretical model to the experimental results, one notes that the two are in very good agreement over most of the spectral range. The experimental results produce the expected zero-reflectance conditions at 550 nm. The theoretical calculations predict an average reflectance of 4.96%, while the measured value of the single-layer AR coating produced in this work was 5.31%. This small discrepancy is due to deviations from the model at wavelengths below 500 nm. At lower wavelengths, the extinction coefficient is small but is not identically zero (34). The model used assumed no absorbance, and this fact may account for the deviation of the experimental data from the model.

A three-layer AR coating was designed to further minimize the reflectance across the full visible spectrum. The three-layer AR coating was produced consisting of TiO_2, SiO_2-TiO_2 alloy, and SiO_2 layers as shown in Figure 7. The design of the three-layer AR coating was optimized with TFCalc using the material properties of the individual constituents. Figure 7 compares the experimental results with the design specifications. The experimental results again show very good agreement with those predicted by the model, with slight deviations from the model occurring at shorter wavelengths. The predicted average reflectance was 2.2%, which compares very favorably with the experimental value of 2.5%. The excellent agreement between the design specifications and experimental results demonstrate the viability of pulsed PECVD for producing optical coatings.

4. CONCLUSIONS

SiO_2-TiO_2 alloys were deposited by pulsed PECVD using $SiCl_4$ and $TiCl_4$ at room temperature. It was found that the growth rate of the alloy films followed a linear combination of the two components, making it straightforward to readily tune the composition and refractive index of alloys between those of the parent materials. These alloys were then used to produce single- and triple-layer AR coatings. Experimental results were in excellent agreement with optimized designs, demonstrating the ability of pulsed PECVD to deliver digital control over both alloy composition and thickness.

Acknowledgment. We gratefully acknowledge the National Science Foundation for partial support of this work through awards CBET-0829043 and CMMI-0826323. Additional funding was provided by the Shared Research Program of the Center for Revolutionary Solar Photoconversion.

REFERENCES AND NOTES

(1) Seman, M.; Robbins, J. J.; Agarwal, S.; Wolden, C. A. *Appl. Phys. Lett.* **2007**, *90*, 131504_1−131504_3.
(2) Seman, M. T.; Robbins, J. J.; Leonhardt, D.; Agarwal, S.; Wolden, C. A. *J. Electrochem. Soc.* **2008**, *155*, J168−J174.
(3) Szymanski, S. F.; Rowlette, P.; Wolden, C. A. *J. Vac. Sci. Technol. A* **2008**, *26*, 1079−1084.
(4) Szymanski, S. F.; Seman, M. T.; Wolden, C. A. *Surf. Coat. Technol.* **2007**, *201*, 8991−8997.
(5) Rowlette, P. C.; Allen, C. G.; Bromley, O. B.; Wolden, C. A. *J. Vac. Sci. Technol. A* **2009**, *27*, 761−766.
(6) Seman, M. T.; Richards, D. N.; Rowlette, P. C.; Kubala, N. G.; Wolden, C. A. *J. Vac. Sci. Technol. A* **2008**, *26*, 1213−1217.
(7) Seman, M. T.; Richards, D. N.; Rowlette, P.; Wolden, C. A. *Chem. Vap. Deposition* **2008**, *14*, 296−302.
(8) Szymanski, S. F.; Seman, M. T.; Wolden, C. A. *J. Vac. Sci. Technol. A* **2007**, *25*, 1493−1499.
(9) Rowlette, P. C.; Canon, M.; Wolden, C. A. *J. Phys. Chem. C.* **2009**, *113*, 6906−6909.
(10) Kubala, N. G.; Rowlette, P. C.; Wolden, C. A. *Electrochem. Solid State Lett.* **2009**, *12*, H259−H262.
(11) Wang, X. R.; Masumoto, H.; Someno, Y.; Hirai, T. *Thin Solid Films* **1999**, *338*, 105−109.
(12) Szczyrbowski, J.; Brauer, G.; Teschner, G.; Zmelty, A. *J. Non-Cryst. Solids* **1997**, *218*, 25−29.
(13) Larouche, S.; Szymanowski, H.; Klemberg-Sapieha, J. E.; Martinu, L.; Gujrathi, S. C. *J. Vac. Sci. Technol. A* **2004**, *22*, 1200−1207.
(14) Lien, S. Y.; Wuu, D. S.; Yeh, W. C.; Liu, J. C. *Sol. Energy Mater. Sol. Cells* **2006**, *90*, 2710−2719.
(15) Wang, X.; Masumoto, H.; Someno, Y.; Hirai, T. *J. Vac. Sci. Technol. A* **1999**, *17*, 206−211.
(16) Wang, X. R.; Masumoto, H.; Someno, Y.; Chen, L. D.; Hirai, T. *J. Vac. Sci. Technol. A* **2000**, *18*, 933−937.

(17) Asghar, M. H.; Placido, F.; Naseem, S. *Opt. Eng.* **2007**, *46*, 023802_1–023802_10.
(18) Poitras, D.; Larouche, S.; Martinu, L. *Appl. Opt.* **2002**, *41*, 5249–5255.
(19) Zhang, X. T.; Fujishima, A.; Jin, M.; Emeline, A. V.; Murakami, T. *J. Phys. Chem. B* **2006**, *110*, 25142–25148.
(20) Hoex, B.; van Erven, A. J. M.; Bosch, R. C. M.; Stals, W. T. M.; Bijker, M. D.; van den Oever, P. J.; Kessels, W. M. M.; van de Sanden, M. C. M. *Prog. Photovoltaics* **2005**, *13*, 705–712.
(21) El Amrani, A.; Menous, I.; Mahiou, L.; Tadjine, R.; Touati, A.; Lefgoum, A. *Renew. Energy* **2008**, *33*, 2289–2293.
(22) Wei, M. C.; Chang, S. J.; Tsia, C. Y.; Liu, C. H.; Chen, S. C. *Sol. Energy* **2006**, *80*, 215–219.
(23) Kern, W.; Tracy, E. *RCA Rev.* **1980**, *41*, 133–180.
(24) Buiu, O.; Lu, Y.; Mitrovic, I. Z.; Hall, S.; Chalker, P.; Potter, R. J. *Thin Solid Films* **2006**, *515*, 623–626.
(25) Pedrotti, F. L.; Pedrotti, L. S.; Pedrotti, L. M. *Introduction To Optics*, 3rd ed.; Prentice Hall: Upper Saddle River, NJ, 2007; pp 476–489.
(26) TFCalc Version 3.4; Software Spectra, Portland, OR, 1999.
(27) Niskanen, A.; Arstila, K.; Leskela, M.; Ritala, M. *Chem. Vap. Deposition* **2007**, *13*, 152–157.
(28) Busani, T.; Devine, R. A. B. *Semicond. Sci. Technol.* **2005**, *20*, 870–875.
(29) Yang, W. L.; Marino, J.; Monson, A.; Wolden, C. A. *Semicond. Sci. Technol.* **2006**, *21*, 1573–1579.
(30) Ricchiardi, G.; Damin, A.; Bordiga, S.; Lamberti, C.; Spano, G.; Rivetti, F.; Zecchina, A. *J. Am. Chem. Soc.* **2001**, *123*, 11409–11419.
(31) Tozzola, G.; Mantegazza, M. A.; Ranghino, G.; Petrini, G.; Bordiga, S.; Ricchiardi, G.; Lamberti, C.; Zulian, R.; Zecchina, A. *J. Catal.* **1998**, *179*, 64–71.
(32) Barr, T. L. *J. Vac. Sci. Technol. A* **1991**, *9*, 1793–1805.
(33) Barr, T. L.; Lishka, M. A. *J. Am. Chem. Soc.* **1986**, *108*, 3178–3186.
(34) Chao, S.; Wang, W. H.; Hsu, M. Y.; Wang, L. C. *J. Opt. Soc. Am. A-Opt. Image Sci. Vis.* **1999**, *16*, 1477–1483.

AM900506Y